Local electrical degradations of solid-state electrolyte by nm-scale *operando* imaging of ionic and electronic transports

C.-S. Jiang[1]* Y. Yin[1], H. Guthrey[1], K. Park[1], S.-H. Lee[2], and M.M. Al-Jassim[1]

[1]National Renewable Energy Laboratory (NREL), Golden, Colorado, USA

[2]Department of Mechanical Engineering, University of Colorado, Boulder, USA

Abstract

We report on degradation mechanisms of solid-state electrolyte (SSE) based on insights from nm-scale ionic conduction and electronic leakage for solid-state batteries. The significantly different local degradations revealed by nm-scale ionic and electronic transport imaging demonstrate the need for this nm-scale investigation. State-of-the-art lithium-ion conductive glass ceramic (Li_2O-Al_2O_3-SiO_2-P_2O_5-TiO_2-GeO_2) SSE shows at least two types of degradations spatially separated within the SSE, namely: 1) ionic conduction blocking and slight electronic leaking and 2) highly electronic shunting. Degradation was significantly suppressed by application of a Li-containing polyacrylonitrile thin coating on both sides of the ceramic SSE. With this coating, the ionic conduction was not reduced by the extensive cycling; instead, it improved slightly, although accompanied by a slight increase in electronic leaking. Our nm-scale transport imaging was achieved using an atomic force microscopy (AFM)-based half-cell setup and a logarithmic-scale amplifier with current sensitivity down to the fA (10^{-15} A) range. This half-cell setup consisting of an AFM-probe/SSE/Li structure can distinguish the ionic from the electronic current by flipping the bias-voltage polarity. This nm-scale *operando* imaging opens up novel characterization of ionic and electronic transport in the field of solid-state batteries.

Key words: solid-state electrolyte; solid-state battery; atomic force microscopy; ionic and electronic transport; degradation

*Corresponding author: chun.sheng.jiang@nrel.gov

1. Introduction

Lithium solid-state batteries (SSBs) are a major focus for safe next-generation, high-density energy storage [1][2][3][4]. The ion conductivity of ceramic solid-state electrolyte (SSE) has been greatly enhanced to a level comparable to that of liquid electrolytes [2][5][6][7], which is critical for fast charging and discharging rates. However, great challenges have been encountered at the SSE/electrode interfaces when integrating the SSE into SSB cells [8]. A major issue is the interface stability that depends on various chemical reactions of the SSE with electrode materials, especially with Li metal, which is the anode material with the highest energy density but which is highly reactive [9][10][11][12]. The chemical reaction usually starts from the interface and can develop deeply into the SSE and electrode bulk, causing device degradation and failure. This instability must be mitigated before the SSB can be competitive at the commercial level. Many studies have proposed to engineer the interfaces by adding an interlayer such as a polymer coating [13], Li salts anchoring [14][15], or a metal interlayer [16]. Unlike ceramic materials, polymer materials show excellent mechanical plasticity and chemical stability when contacting Li metal. Therefore, polymers containing Li salts were considered as promising candidates for stabilizing the interface [17][18][19]. The ion conductivity of polymer electrolyte is usually much lower than that of ceramic electrolyte, thus the polymer interlayer should be adequately thin to reduce the resistance for ion transport across the interface.

A significant improvement in the stability and cyclability of a state-of-the-art ceramic electrolyte—a commercial Li-ion conductive glass ceramic (LICGC)—was reported by coating a polyacrylonitrile (PAN) thin layer [20]. The galvanostatic cycling data show stable or even improved conductivity with the cycling. In contrast, the LICGC without the coating shows degraded conductivity due to extensive cycling. The interface reaction caused the performance degradation, as identified by the color change of the ceramic-

only SSE from its initial white to black after the cycling, whereas the SSE with the coating shows no change in the color and thus probably no significant interface reaction [20]. The direct macroscopic electrical data such as galvanostatic cycling and electrochemical impedance spectroscopy (EIS) are the main tool for testing and assessing battery cells in the SSB community [20][21][22][23]. A crucial question that arises is how the averaged electrical data from the macroscopic testing reflect the real operation and degradation mechanisms of battery cells, which can be highly nonuniform at the micro- or even nanometer scale. For example, is degraded electronic leakage of SSE caused by local heavy shunting or by large-area uniform degradation? An answer to this question is much needed for SSB development. However, despite extensive microscopic morphological, chemical, and structural characterizations [21][22][23], there have been no literature reports of degradation mechanisms by direct microscopic electrical characterization.

We have developed an atomic force microscopy (AFM)-based nm-resolution electrical imaging technique for charge transport through SSEs; it uses a half-cell setup consisting of AFM-probe/SSE/electrode. This technique allows us to distinguish the ionic current and electronic current by flipping the bias-voltage polarity. Using this technique, we have found highly nonuniform ion conduction of Li_3PS_4 (LPS) polycrystalline ceramic and LPS/polymer bulk hybrid SSEs[24]. Here, we report on the microscopic degradation mechanisms of LICGC as revealed by this nm-scale *operando* technique. We found highly complicated electrical degradations varying in micrometer to submillimeter sizes depending on the local domains. In contrast, the polymer-coated LICGC shows uniform improvement of ionic conduction, but slight, uniform electronic degradation due to the extensive cycling.

2. Results and Discussions

The half-cell setup for imaging the charge transport through SSE is shown in Fig. 1. The AFM probe is scanned over the SSE surface in contact mode. A bias voltage (Vs) is applied to the Li metal and the probe is virtually grounded, with the potential kept the same as the ground level but not actually grounded so that the electrical current flowing through the probe can be measured. We used a logarithmic-scale amplifier to

enhance the current sensitivity in the mA–fA (10^{-3}–10^{-15} A) range; this enabled the detection of both ionic and electronic current, respectively, in the pA and fA ranges flowing through the probe with an ~100-nm radius. When a negative Vs is applied, only the electronic leaking current flows through the SSE (Fig. 1a), because Li+ ionic current is blocked at the steady state with this bias, neither a Li atom is available from the probe side flowing to the Li metal side nor a Li ion in the SSE can be reduced to a Li atom by a Vs less than -1 V [25][26][27]. With a positive Vs applied, both ionic and electronic current can flow. Because the electronic current should be approximately symmetrical with the negative and positive Vs, ionic and electronic currents can be identified by measuring and comparing the currents in both polarities. In a working SSE, the ionic current is many orders of magnitude larger than the electronic current; so, ionic current dominates the measured current with a positive Vs. However, in a degraded SSE, electronic conduction can be comparable to or even larger than the ionic conduction; current images are taken with both polarities to assess the electrical transport.

We first show charge-transport imaging on the pristine ceramic-only SSE, then discuss in detail the SSE degradation mechanisms by taking current images on degraded SSE. Finally, we will show both the pristine and cycled SSE with polymer coating.

2.1 Pristine ceramic SSE

The commercial pristine LICGC SSE with glass ceramic components of Li_2O-Al_2O_3-SiO_2-P_2O_5-TiO_2-GeO_2 [28] appears uniform and shiny in optical microscope images (Fig. 2a), and the surface is flat as shown by the AFM image (Fig. 2b), which has a root-mean-square roughness of 1.2 nm. The average ion current is 2.5 pA with a positive Vs = +0.5 V, as indicated in the middle of the logarithmic scale bar (Fig. 2c). The current shows significant fluctuation, with amplitude comparable to the average current value (Fig. 2d). The sizes of the regions with different current signals are about 100 nm to 1 μm. Both the amplitude and length scale of current fluctuations are much smaller than that of the polycrystalline LPS SSE, which has 1–2 orders-of-magnitude fluctuation in ion current amplitude and a length scale of several hundreds of nm

to several μm[24]. This relatively small current fluctuation should be due to the glass ceramic structure, which has smaller grain sizes [28][29] in its amorphous matrix compared with the hundreds of nm grain size and several μm agglomerate sizes of the polycrystalline LPS SSE [24][30]. The AFM-based half-cell setup primarily probes the electrical conductivity in the local areas beneath the probe. The current routes spread rapidly with distancing from the local area, and the Vs drop is dominated on the local nm-scale volume of the material, which ensures the nm-scale resolution of the technique [31][32][33]. The current density flowing through the probe is 2.5 pA/$\pi r^2 \sim 8$ mA/cm^2 with nominal probe radius r of ~100 nm, which is compatible with or slightly higher than the normal charging/discharging rate of a battery.

The electronic leaking current with a negative Vs = -0.5 V is 5 orders of magnitude smaller than the current at Vs = +0.5 V (Figs. 2e and 2f) and fluctuates in amplitude similar to the current value. The electronic conduction of ceramic materials should be approximately symmetrical about the Vs polarity, i.e., the electronic current at Vs = +0.5 V should be about 5 orders of magnitude smaller than the measured current, which is the sum of the electronic and ionic currents. So, the measured current is dominated by the ionic current. This electronic conduction can be caused by electronic-state overlapping between defects inside the SSE. Although the ceramic material is fundamentally an electronic insulator, the wavefunctions of defect states can overlap and form conduction percolation paths[34][35]. Another conduction mechanism is redox transition of the multiple bonding states in the highly disordered ceramic material containing multiple components. Electron transport can be dominated by the redox of multi-bonding states through crystalline structures without defects. In the current experimental setting, Li metal is attached to one side of the SSE and can reduce Ti^{4+} to Ti^{3+} even without any electrochemical cycling. Although the reduction is not visually obvious, local reduction can increase electronic conductivity. Apparently, the 5 orders-of-magnitude smaller electronic conduction is not small enough to block Li dendrite growth from the SSE bulk. This degree of electronic conduction can supply electrons to reduce Li ions needed for Li dendrite growth inside the SSE bulk. Therefore, further suppression of the electronic conduction is needed to eliminate the Li dendrite growth.

2.2 Degradation of ceramic SSE

After extensive cycling of the Li/SSE/Li half-cell with 360 cycles, one side of the Li metal was mechanically removed, and the SSE surface was exposed to be characterized. Apparent color of the SSE is black, which is indicative of significant chemical reactions due to the cycling [20]. Optical microscopy inspection shows the SSE to be a mixture of bright and dark irregular shapes, with sizes ranging from micrometers to submillimeter. This variety indicates that the chemical reaction might be highly nonuniform. We have carried out a relatively comprehensive survey of the various domains using the AFM-based transport imaging. The results, as follow, indicate highly different degradation mechanisms involving ionic and electronic conduction and insulation.

First, we show some areas that are not degraded in either ionic conduction or electronic insulation (Fig. 3). This type of area (type 1) is in a small portion of the whole area—probably less than 10%. The optical image shows as relatively bright, with surrounding dark areas (Fig. 3a). Surface morphology was roughened to a moderate degree by the cycling (Fig. 3b). The ion conduction was somewhat improved in several times rather than degraded (Fig. 3c). However, the ion current fluctuation also increased several times to about one order of magnitude. The electronic conduction remains similar to the pristine state. Although the average electronic current (Fig. 3e) is smaller than that of the pristine state (Fig. 2e), the amplifier output at this small current value is not accurate because of the narrow bandwidth. Only the qualitative scale in the same current images and the rough orders of magnitude are reliable. Overall, the type 1 area shows very similar transport properties to the pristine SSE and has not been apparently affected by the electrochemical cycling.

Next, we show different degradations. The most typical degradation (type 2), across more than 80% of the area, is shown in Fig. 4. Optical images on this type of area are dark, and AFM surface morphology is rough with corrugations of ~1 μm. The current at positive Vs decreased about two orders of magnitude, whereas the current at negative Vs increased two orders of magnitude; so, the currents at both polarities are

comparable. This illustrates that both the ionic conduction and electronic insulation were degraded, and the electronic current can dominate both the images. The galvanostatic cycling data (see Supplemental Materials Fig. S1) show monotonically increased voltage with cycling, which is mainly caused by this degradation in the charge transports. The voltage polarization during Li plating/stripping (>200 cycles) may be mainly due to ohmic resistance for the electronic conduction. This result is important because the rectangular-shaped galvanostatic voltage curves could give wrong indication that the SSE is still working as a Li^+ solid electrolyte. Here, we were able to show with the AFM-based half-cell setup that the voltage curves should be understood with the electronic transports instead of the ionic transports. However, what chemical reaction caused the ionic blocking and electronic conduction increase cannot be assessed directly by this transport imaging.

Type 3 degradation shows very high electronic conduction (Fig. 5). The optical image shows bright areas and AFM shows moderately roughened surface morphology (Fig. 5b). Domain sizes of this type of degradation are usually small and adjacent to areas of type 2 degradation. Figure 5 shows images taken across both type 3 (left) and type 2 (right). The current images with the opposite polarities show similar current amplitudes in both the regions, with very high current of 10^2–10^3 pA orders on the left (type 3) and low current of 10^{-2}–10^{-3} pA orders on the right (type 2). Again, this current image is dominated by electronic but not ionic conduction because of the similar values with the opposite polarities.

This type of degradation can raise a crucial question: What reaction caused the local ceramic electronic insulator to change to highly electronic conductive? Further, the mixture of type 2 and type 3 degradations can be found to be highly blended and with small μm domain sizes. An example is shown in Fig. S2 with a domain size of several μm. The surface morphology is relatively rough (Fig. S2b), and the optical image (Fig. S2a) shows a very small bright dot surrounded by darkness. The degree of electronic leaking in type 2 degradation is relatively weak (10^{-3}–10^{-2} pA), but the degradation area is more than 80%. On the other hand, the leaking current of type 3 degradation is huge (10^2–10^3 pA), but the degradation area can be in a very small portion of the SSE. The ionic conduction in the degraded SSE is largely blocked, and electronic

leaking can dominate the galvanostatic data. Although the degradation mode should be proposed by local materials chemical analyses, it could be partly interpreted by the materials specification of the LICGC SSE (28). LICGC is composed of three crystallographic phases, $Li_{1+x}Al_xGe_yTi_{2-x-y}P_3O_{12}$ as a main phase, and $AlPO_4$ and $Li_{1+x+3z}Al_x(Ge,Ti)_{2-x}(Si_zPO_4)_3$ as sub phases. The type 2 area can be assigned to the main phase, $Li_{1+x}Al_xGe_yTi_{2-x-y}P_3O_{12}$, because (i) it is the main area covering more than 80% of the whole sample area and (ii) Ti^{4+} can be reduced to Ti^{3+} by accepting Li^+/e^- from Li metal, which increase electronic conductivity through the $Ti^{4+/3+}$ redox couple and the color change from white to black[36][37]. The type 1 should be then $AlPO_4$ because there is no notable electronic conductivity increase by the cycling, which is a signature of Ti-free domains. The other sub-phase, $Li_{1+x+3z}Al_x(Ge,Ti)_{2-x}(Si_zPO_4)_3$ can be assigned to the type 3 domain based on its size and the large electronic conductivity increase. Detailed mechanisms of nm-scale distribution of ionic conduction blocking and electronic leakage seem to depend on the crystallographic structure and morphology of the solid electrolyte[38][39][40], such as atomic defects (Schottky defects[41], Frenkel defects[42]) and crystallite size, which request further investigations using methods beyond the AFM-based electrical imaging techniques.

We have found at least the two types of degraded areas and non-degraded areas on the degraded SSE, with the dominance of type 2 where the ion conduction is blocked and the electronic leaking is slightly increased. This nm-scale transport imaging provides assessment of the electrical degradation, which is directly related to the Li plating and stripping in the half-cell. Further understanding what lies behind the electrical behavior requires local microscopic chemical and structural characterization.

2.3 Polymer-coated SSE

We have reported that the stability and cyclability of the half-cell were significantly improved by the Li-containing PAN coating on the ceramic SSE. The galvanostatic data showed the initial decreased electrical conduction compared with the SSE without polymer coating; but the electrical conductivity increased by extensive charging/discharging of 360 cycles (see Fig. S1), in contrast to the reduced conductivity of the

ceramic-only SSE. The nm-transport imaging on the pristine polymer-coated SSE (Fig. 6) shows reduced ionic conductivity (Figs. 6c and 6d) by about one order of magnitude compared with the ceramic-only SSE (Figs 2c and 2d), which is consistent with the galvanostatic data (Fig.S1). This reduced current is due to the thin coating of ~10 μm on both sides of the ceramic SSE. The ion current is distributed relatively uniformly, and the current fluctuation is moderate with an amplitude similar to the current value. The electronic leaking current is also relatively uniform and in the 10^{-5} pA range, similar to the leaking current without the coating. The ionic current dominates electrical conduction on the working polymer-coated SSE with a positive Vs.

After the extensive cycling, the SSE does not show a significant chemical reaction with Li metal, unlike the ceramic-only SSE. The optical microscopy (Fig. 7a) shows a bright image except for local scattered dark spots that are in a small portion of the image. The AFM image (Fig. 7b) shows a moderately roughened surface morphology after the cycling. The ion current increased from 0.6 pA to 1.3 pA, about double the current value due to the cycling. The current fluctuation also increased to slightly larger than the current value. This increase of ionic conduction is probably due to the improved polymer/Li contact and adhesion due to the cycling. At the same time, the electronic leaking current increased more than two orders of magnitude. Still, the electronic leaking current is two orders of magnitude smaller than the ionic current, and ionic current dominates the current image with the positive Vs, showing that the SSE is working after the cycling. The result confirms that the voltage polarization during galvanostatic cycling (Fig. S1) is mainly originated from the ionic transport limitations during cycling unlike the bare SSE case. It is interesting to note that the degree of the voltage polarization of the polymer-coated SSE is similar to that of the bare SSE (Fig. S1; after 200 cycles), which indicates that the resistance of Li^+ transports in the polymer-coated SSE is similar to that of the electronic transports in the bare SSE with degradations. This further emphasize the importance of the *operando* AFM-based analysis of ionic and electronic transports because it can deconvolute galvanostatic voltage signals to the electronic and ionic current components.

3. Conclusion

We have performed a detailed study of SSE degradation mechanisms by assessing nm-scale ionic and electronic transport. The highly nonuniform and significantly different transport mechanisms in both the ionic conduction and electronic leaking demonstrate the need for nm-scale investigation, which provides insight far beyond macroscopic characterization. The ceramic SSE degradation with extensive cycling is caused by different local mechanisms—including, but not limited to, ion conduction blocking combined with slight electronic leaking as well as local highly electronic shunting. With a thin polymer coating, the degradation was effectively suppressed, and the ion conduction was even slightly improved although a slight electronic degradation was also detected due to the cycling. These results illustrate that the nm-scale current imaging opens up novel, important characterization for ionic and electronic transport in the field of solid-state batteries.

4. Materials and Methods

Nanometer-scale charge-transport imaging. The nm-scale ionic and electronic charge-transport imaging was conducted on the electrolyte surfaces based on contact-mode AFM (Veeco D5000 and Nanoscope V) in an Ar glovebox. The AFM-probe/electrolyte/Li-metal setup forms a half-cell that is in the *operando* state during transport imaging. A Vs was applied to the Li metal side, and the probe was kept at the ground potential level, but not connected to the ground in order to measure the current flowing through the probe. We used a logarithmic current amplifier to enhance the current sensitivity in a wide range of mA~fA orders. A diamond-coated Si probe (BrukerNano DDESP) was employed for strong wear-off resistance. Constant contact force between the probe and sample was controlled in a moderate force level of tens of nN to ensure both good contact and that the sample was not damaged. Scanning speed of the probe was set at ~500 nm/s to leverage the imaging quality and productivity. Some minor topographic effect of the current imaging was observed and examined when scanning on rough sample surfaces.

SSE sample preparation. The state-of-the-art ceramic electrolyte (LICGC^{TM} AG-01) was acquired from OHARA Inc. (Japan). The plate-shaped SSE has a diameter of 19 mm and a thickness of 0.15 mm, with

compositions of Li_2O-Al_2O_3-SiO_2-P_2O_5-TiO_2-GeO_2. The ceramic electrolyte was dried at 100°C for 20 hours before being assembled to a Li/SSE/Li half-cell. To make the polymer coating on the ceramic SSE, we dissolved $LiClO_4$ powders and PAN powders (average molecular weight of 150,000) into dimethylformamide (DMF) solvent with a ratio at 1:9:90 by weight. DMF, PAN, and $LiClO_4$ powders were acquired from Sigma-Aldrich Corporation (USA). The gel was coated on both sides of the ceramic electrolyte by dipping the ceramic sample into the gel for 10 seconds and drying it for 20 hours at room temperature, forming a polymer/LiCGC/polymer sandwich structure. The polymer-coating thickness was ~10 μm as measured by a micrometer before and after the coating. The polymer electrolyte coating contains 10% $LiClO_4$ by weight in PAN.

Electrochemical test. An electrochemical cell with the structure of Li/polymer/LiCGC/polymer/Li was tightly clamped by a pressing tool and then rested for 24 hours before the electrochemical cycling test. The Li metal electrode was punched into a round shape with a 9/16-inch diameter from Li metal foil. The Li metal foil was acquired from Alfa Aesar with the thickness of 0.75 mm and purity of 99.9% (metals basis), and it was scratched by a sharp blade to expose a shiny surface before use. An electrochemical cell with the structure of Li/LICGC/Li was also constructed as a control sample. The voltage profile of Li stripping and plating cycling were measured by using Bio-Logic Science Instruments SAS (VMP3).

Acknowledgment

The authors acknowledge funding support by the Laboratory Directed Research and Development (LDRD) program at NREL. This work was supported by the U.S. Department of Energy under Contract No. DE-AC36-08GO28308 with the Alliance for Sustainable Energy, LLC, the Manager and Operator of the National Renewable Energy Laboratory. Funding was provided by the U.S. Department of Energy Office of Energy Efficiency and Renewable Energy Solar Energy Technologies Office. The U.S. Government retains and the publisher, by accepting the article for publication, acknowledges that the U.S.

References

[1] P.H.L. Notten, F. Roozeboom, R. a. H. Niessen, L. Baggetto, 3-D Integrated All-Solid-State Rechargeable Batteries, Advanced Materials. 19 (2007) 4564–4567. https://doi.org/10.1002/adma.200702398.

[2] J. Trevey, J.S. Jang, Y.S. Jung, C.R. Stoldt, S.-H. Lee, Glass–ceramic Li2S–P2S5 electrolytes prepared by a single step ball billing process and their application for all-solid-state lithium–ion batteries, Electrochemistry Communications. 11 (2009) 1830–1833. https://doi.org/10.1016/j.elecom.2009.07.028.

[3] K. (Kelvin) Fu, Y. Gong, B. Liu, Y. Zhu, S. Xu, Y. Yao, W. Luo, C. Wang, S.D. Lacey, J. Dai, Y. Chen, Y. Mo, E. Wachsman, L. Hu, Toward garnet electrolyte–based Li metal batteries: An ultrathin, highly effective, artificial solid-state electrolyte/metallic Li interface, Science Advances. 3 (2017) e1601659. https://doi.org/10.1126/sciadv.1601659.

[4] W. Luo, Y. Gong, Y. Zhu, Y. Li, Y. Yao, Y. Zhang, K. (Kelvin) Fu, G. Pastel, C.-F. Lin, Y. Mo, E.D. Wachsman, L. Hu, Reducing Interfacial Resistance between Garnet-Structured Solid-State Electrolyte and Li-Metal Anode by a Germanium Layer, Advanced Materials. 29 (2017) 1606042. https://doi.org/10.1002/adma.201606042.

[5] P. Knauth, Inorganic solid Li ion conductors: An overview, Solid State Ionics. 180 (2009) 911–916. https://doi.org/10.1016/j.ssi.2009.03.022.

[6] V. Thangadurai, S. Narayanan, D. Pinzaru, Garnet-type solid-state fast Li ion conductors for Li batteries: critical review, Chemical Society Reviews. 43 (2014) 4714–4727. https://doi.org/10.1039/C4CS00020J.

[7] J.C. Bachman, S. Muy, A. Grimaud, H.-H. Chang, N. Pour, S.F. Lux, O. Paschos, F. Maglia, S. Lupart, P. Lamp, L. Giordano, Y. Shao-Horn, Inorganic Solid-State Electrolytes for Lithium Batteries: Mechanisms and Properties Governing Ion Conduction, Chem. Rev. 116 (2016) 140–162. https://doi.org/10.1021/acs.chemrev.5b00563.

[8] W. Zhao, J. Yi, P. He, H. Zhou, Solid-State Electrolytes for Lithium-Ion Batteries: Fundamentals, Challenges and Perspectives, Electrochem. Energ. Rev. 2 (2019) 574–605. https://doi.org/10.1007/s41918-019-00048-0.

[9] S. Wenzel, D.A. Weber, T. Leichtweiss, M.R. Busche, J. Sann, J. Janek, Interphase formation and degradation of charge transfer kinetics between a lithium metal anode and highly crystalline Li7P3S11 solid electrolyte, Solid State Ionics. 286 (2016) 24–33. https://doi.org/10.1016/j.ssi.2015.11.034.

[10] J. Lau, R.H. DeBlock, D.M. Butts, D.S. Ashby, C.S. Choi, B.S. Dunn, Sulfide Solid Electrolytes for Lithium Battery Applications, Advanced Energy Materials. 8 (2018) 1800933. https://doi.org/10.1002/aenm.201800933.

[11] T. Swamy, X. Chen, Y.-M. Chiang, Electrochemical Redox Behavior of Li Ion Conducting Sulfide Solid Electrolytes, Chem. Mater. 31 (2019) 707–713. https://doi.org/10.1021/acs.chemmater.8b03420.

[12] Y. Zhu, X. He, Y. Mo, Origin of Outstanding Stability in the Lithium Solid Electrolyte Materials: Insights from Thermodynamic Analyses Based on First-Principles Calculations, ACS Appl. Mater. Interfaces. 7 (2015) 23685–23693. https://doi.org/10.1021/acsami.5b07517.

[13] Y. Li, H. Xu, P.-H. Chien, N. Wu, S. Xin, L. Xue, K. Park, Y.-Y. Hu, J.B. Goodenough, A Perovskite Electrolyte That Is Stable in Moist Air for Lithium-Ion Batteries, Angewandte Chemie International Edition. 57 (2018) 8587–8591. https://doi.org/10.1002/anie.201804114.

[14] C. Luo, X. Ji, J. Chen, K.J. Gaskell, X. He, Y. Liang, J. Jiang, C. Wang, Solid-State Electrolyte Anchored with a Carboxylated Azo Compound for All-Solid-State Lithium Batteries, Angewandte Chemie International Edition. 57 (2018) 8567–8571. https://doi.org/10.1002/anie.201804068.
[15] R. Xu, F. Han, X. Ji, X. Fan, J. Tu, C. Wang, Interface engineering of sulfide electrolytes for all-solid-state lithium batteries, Nano Energy. 53 (2018) 958–966. https://doi.org/10.1016/j.nanoen.2018.09.061.
[16] K. (Kelvin) Fu, Y. Gong, Z. Fu, H. Xie, Y. Yao, B. Liu, M. Carter, E. Wachsman, L. Hu, Transient Behavior of the Metal Interface in Lithium Metal–Garnet Batteries, Angewandte Chemie International Edition. 56 (2017) 14942–14947. https://doi.org/10.1002/anie.201708637.
[17] Enhancing ionic conductivity in composite polymer electrolytes with well-aligned ceramic nanowires | Nature Energy, (n.d.). https://www.nature.com/articles/nenergy201735 (accessed March 22, 2020).
[18] N.-W. Li, Y. Shi, Y.-X. Yin, X.-X. Zeng, J.-Y. Li, C.-J. Li, L.-J. Wan, R. Wen, Y.-G. Guo, A Flexible Solid Electrolyte Interphase Layer for Long-Life Lithium Metal Anodes, Angewandte Chemie International Edition. 57 (2018) 1505–1509. https://doi.org/10.1002/anie.201710806.
[19] Q. Pan, D.M. Smith, H. Qi, S. Wang, C.Y. Li, Hybrid Electrolytes with Controlled Network Structures for Lithium Metal Batteries, Advanced Materials. 27 (2015) 5995–6001. https://doi.org/10.1002/adma.201502059.
[20] Y. Yin, C.-S. Jiang, H. Guthrey, C. Xiao, N. Seitzman, C. Ban, M. Al-Jassim, Improved Stability and Cyclability of Ceramic Solid Electrolyte by Coating Polymer, J. Electrochem. Soc. 167 (2020) 020519. https://doi.org/10.1149/1945-7111/ab68c7.
[21] H. Koshikawa, S. Matsuda, K. Kamiya, M. Miyayama, Y. Kubo, K. Uosaki, K. Hashimoto, S. Nakanishi, Electrochemical impedance analysis of the Li/Au-Li7La3Zr2O12 interface during Li dissolution/deposition cycles: Effect of pre-coating Li7La3Zr2O12 with Au, Journal of Electroanalytical Chemistry. 835 (2019) 143–149. https://doi.org/10.1016/j.jelechem.2019.01.025.
[22] J.A. Lewis, F.J.Q. Cortes, M.G. Boebinger, J. Tippens, T.S. Marchese, N. Kondekar, X. Liu, M. Chi, M.T. McDowell, Interphase Morphology between a Solid-State Electrolyte and Lithium Controls Cell Failure, ACS Energy Lett. 4 (2019) 591–599. https://doi.org/10.1021/acsenergylett.9b00093.
[23] R. Inada, S. Yasuda, H. Hosokawa, M. Saito, T. Tojo, Y. Sakurai, Formation and Stability of Interface between Garnet-Type Ta-doped Li7La3Zr2O12 Solid Electrolyte and Lithium Metal Electrode, Batteries. 4 (2018) 26. https://doi.org/10.3390/batteries4020026.
[24] C.-S. Jiang, N. Dunlap, Y. Li, H. Guthrey, P. Liu, S.-H. Lee, M.M. Al-Jassim, Nonuniform Ionic and Electronic Transport of Ceramic and Polymer/Ceramic Hybrid Electrolyte by Nanometer-Scale Operando Imaging for Solid-State Battery, Advanced Energy Materials. 10 (2020) 2000219. https://doi.org/10.1002/aenm.202000219.
[25] N.D. Lepley, N. a. W. Holzwarth, Computer Modeling of Crystalline Electrolytes: Lithium Thiophosphates and Phosphates, J. Electrochem. Soc. 159 (2012) A538–A547. https://doi.org/10.1149/2.jes113225.
[26] N.D. Lepley, N.A.W. Holzwarth, Y.A. Du, Structures, Li^{+} mobilities, and interfacial properties of solid electrolytes Li${}_{3}$PS${}_{4}$ and

Li${}_{3}$PO${}_{4}$ from first principles, Phys. Rev. B. 88 (2013) 104103. https://doi.org/10.1103/PhysRevB.88.104103.
[27] Y. Yang, Q. Wu, Y. Cui, Y. Chen, S. Shi, R.-Z. Wang, H. Yan, Elastic Properties, Defect Thermodynamics, Electrochemical Window, Phase Stability, and Li+ Mobility of Li3PS4: Insights from First-Principles Calculations, ACS Appl. Mater. Interfaces. 8 (2016) 25229–25242. https://doi.org/10.1021/acsami.6b06754.
[28] K. Nakajima, T. Katoh, Y. Inda, B. Hoffman, Lithium Ion Conductive Glass Ceramics: Properties and Application in Lithium Metal Batteries, (2010) 28.
[29] A. Gurung, J. Pokharel, A. Baniya, R. Pathak, K. Chen, B. Sagar Lamsal, N. Ghimire, W.-H. Zhang, Y. Zhou, Q. Qiao, A review on strategies addressing interface incompatibilities in inorganic all-solid-state lithium batteries, Sustainable Energy & Fuels. 3 (2019) 3279–3309. https://doi.org/10.1039/C9SE00549H.
[30] C.-S. et al. Jiang, Nonuniform Ionic and Electronic Transport of Ceramic and Polymer/Ceramic Hybrid Electrolyte by Nanometer-Scale Operando Imaging for Solid-State Battery, Advanced Energy Materials. Accepted (2020).
[31] P. Eyben, M. Xu, N. Duhayon, T. Clarysse, S. Callewaert, W. Vandervorst, Scanning spreading resistance microscopy and spectroscopy for routine and quantitative two-dimensional carrier profiling, Journal of Vacuum Science & Technology B: Microelectronics and Nanometer Structures Processing, Measurement, and Phenomena. 20 (2002) 471–478. https://doi.org/10.1116/1.1424280.
[32] L. Zhang, K. Ohuchi, K. Adachi, K. Ishimaru, M. Takayanagi, A. Nishiyama, High-resolution characterization of ultrashallow junctions by measuring in vacuum with scanning spreading resistance microscopy, Appl. Phys. Lett. 90 (2007) 192103. https://doi.org/10.1063/1.2736206.
[33] C. Stetson, T. Yoon, J. Coyle, W. Nemeth, M. Young, A. Norman, S. Pylypenko, C. Ban, C.-S. Jiang, M. Al-Jassim, A. Burrell, Three-dimensional electronic resistivity mapping of solid electrolyte interphase on Si anode materials, Nano Energy. 55 (2019) 477–485. https://doi.org/10.1016/j.nanoen.2018.11.007.
[34] B. Zhu, X. Luo, C. Xia, I. Albinsson, B.-E. Mellander, Electrical properties of ZrO2-CeO2 at intermediate temperatures, Ionics. 3 (1997) 363–367. https://doi.org/10.1007/BF02375711.
[35] Y.-T. Chen, A. Jena, W.K. Pang, V.K. Peterson, H.-S. Sheu, H. Chang, R.-S. Liu, Voltammetric Enhancement of Li-Ion Conduction in Al-Doped Li7–xLa3Zr2O12 Solid Electrolyte, J. Phys. Chem. C. 121 (2017) 15565–15573. https://doi.org/10.1021/acs.jpcc.7b04004.
[36] M.-S. Song, A. Benayad, Y.-M. Choi, K.-S. Park, Does Li4Ti5O12 need carbon in lithium ion batteries? Carbon-free electrode with exceptionally high electrode capacity, Chem. Commun. 48 (2011) 516–518. https://doi.org/10.1039/C1CC16462G.
[37] M. Wagemaker, D.R. Simon, E.M. Kelder, J. Schoonman, C. Ringpfeil, U. Haake, D. Lützenkirchen-Hecht, R. Frahm, F.M. Mulder, A Kinetic Two-Phase and Equilibrium Solid Solution in Spinel Li4+xTi5O12, Advanced Materials. 18 (2006) 3169–3173. https://doi.org/10.1002/adma.200601636.
[38] P.H. Kuo, J. Du, Lithium Ion Diffusion Mechanism and Associated Defect Behaviors in Crystalline Li1+xAlxGe2–x(PO4)3 Solid-State Electrolytes, J. Phys. Chem. C. 123 (2019) 27385–27398. https://doi.org/10.1021/acs.jpcc.9b08390.

[39] P. Gorai, H. Long, E. Jones, S. Santhanagopalan, V. Stevanović, Defect chemistry of disordered solid-state electrolyte Li 10 GeP 2 S 12, Journal of Materials Chemistry A. 8 (2020) 3851–3858. https://doi.org/10.1039/C9TA10964A.
[40] A.G. Squires, D.O. Scanlon, B.J. Morgan, Native Defects and Their Doping Response in the Lithium Solid Electrolyte Li7La3Zr2O12, Chem. Mater. 32 (2020) 1876–1886. https://doi.org/10.1021/acs.chemmater.9b04319.
[41] J.A. Dawson, H. Chen, M.S. Islam, Composition Screening of Lithium- and Sodium-Rich Anti-Perovskites for Fast-Conducting Solid Electrolytes, J. Phys. Chem. C. 122 (2018) 23978–23984. https://doi.org/10.1021/acs.jpcc.8b08208.
[42] L. Yin, H. Yuan, L. Kong, Z. Lu, Y. Zhao, Engineering Frenkel defects of anti-perovskite solid-state electrolytes and their applications in all-solid-state lithium-ion batteries, Chemical Communications. 56 (2020) 1251–1254. https://doi.org/10.1039/C9CC08382K.

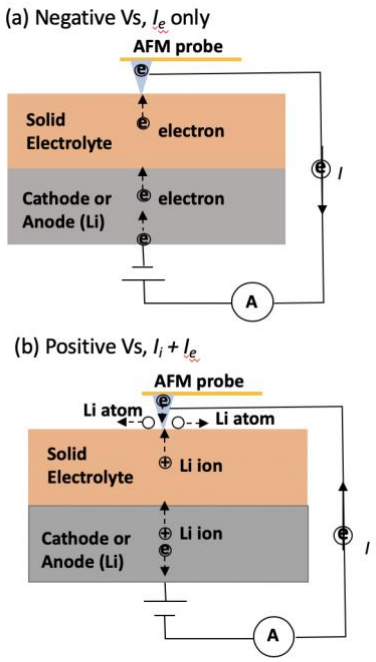

Fig. 1. Schematics illustrating the half-cell setup for charge-transport imaging (a) with a negative Vs polarity that flows only the electronic current, and (b) with a positive Vs that flows both ionic and electronic currents. The ionic and electronic currents are identified by comparing the current at positive and negative Vs values.

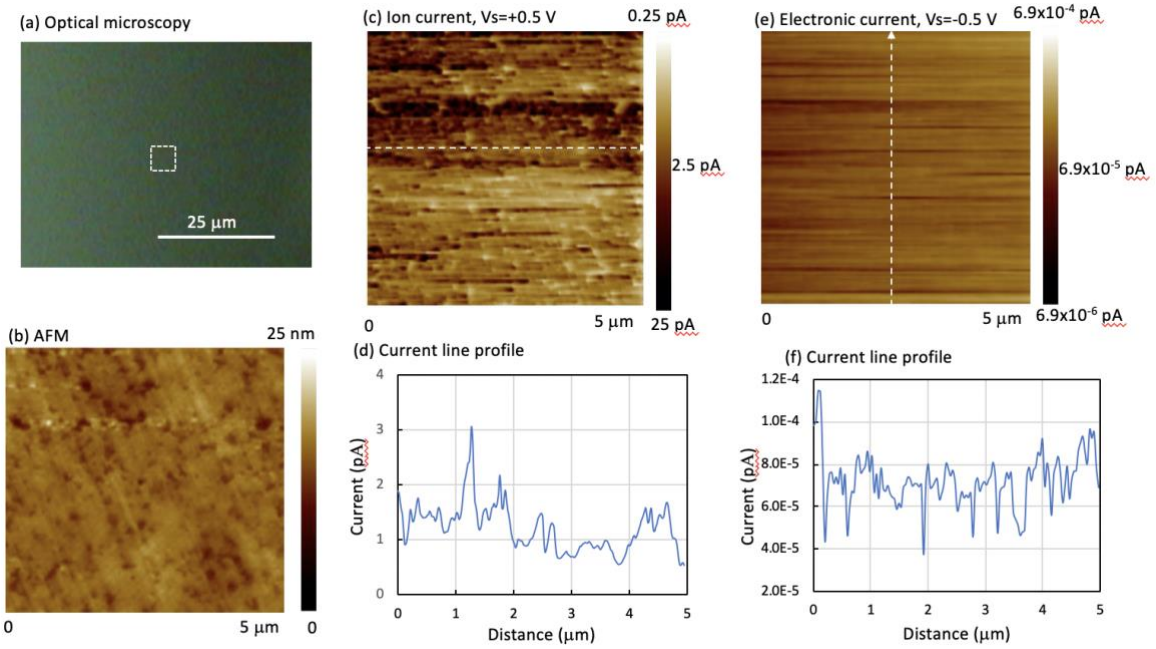

Fig. 2. Transport imaging of the pristine LICGC ceramic-only SSE; (a) an optical microscopy image; (b) an AFM surface morphology image simultaneously taken with the current images; (c) an ionic current image taken with Vs = +0.5 V on the area as indicated by the square in the center of the optical image; (d) a current line profile along the line in (c); (e) an electronic current image taken with Vs = -0.5 V in the same area as (b) and (c); and (f) a current line profile along the line in (e).

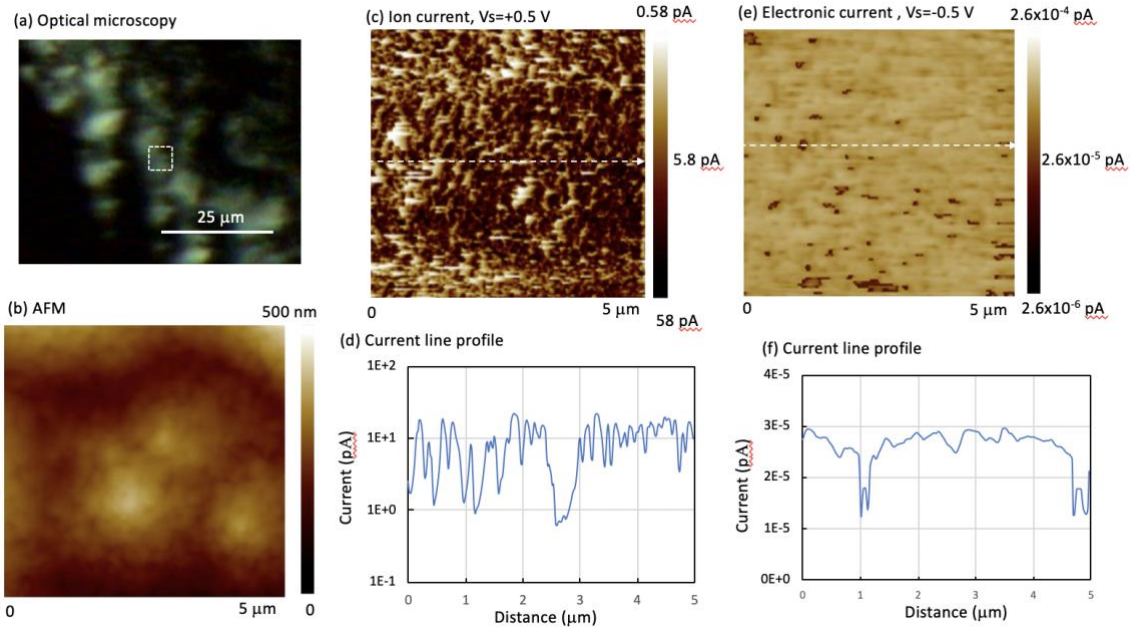

Fig. 3. Charge-transport images taken on a non-degraded area of the LICGC ceramic-only SSE after extensive cycling; (a) an optical microscopy image around this area; (b) an AFM surface morphology image simultaneously taken with the current images; (c) an ionic current image taken with Vs = +0.5 V on the area as indicated by the square in the center of the optical image; (d) a current line profile along the line in (c); (e) an electronic current image taken with Vs = -0.5 V in the same area as (b) and (c); and (f) a current line profile along the line in (e).

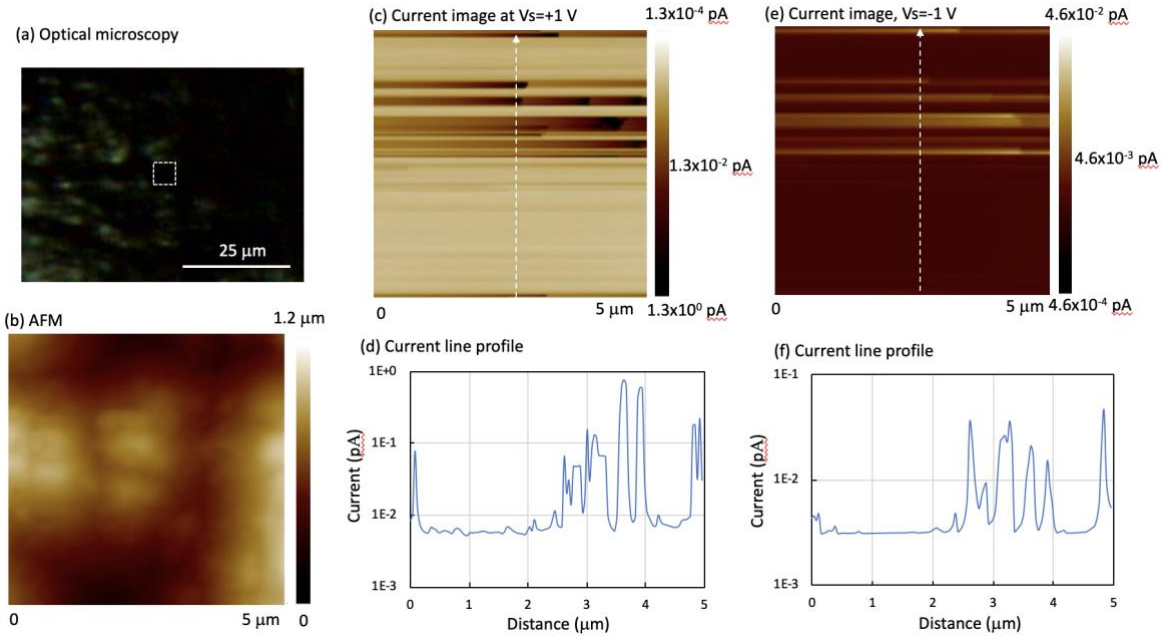

Fig. 4. Charge-transport images taken on a typical degraded area of the LICGC ceramic-only SSE after extensive cycling; (a) an optical microscopy image around this area; (b) an AFM surface morphology image simultaneously taken with the current images; (c) a current image taken with Vs = +1 V on the area as indicated by the square in the center of the optical image; (d) a current line profile along the line in (c); (e) a current image taken with Vs = -1 V in the same area as (b) and (c); and (f) a current line profile along the line in (e).

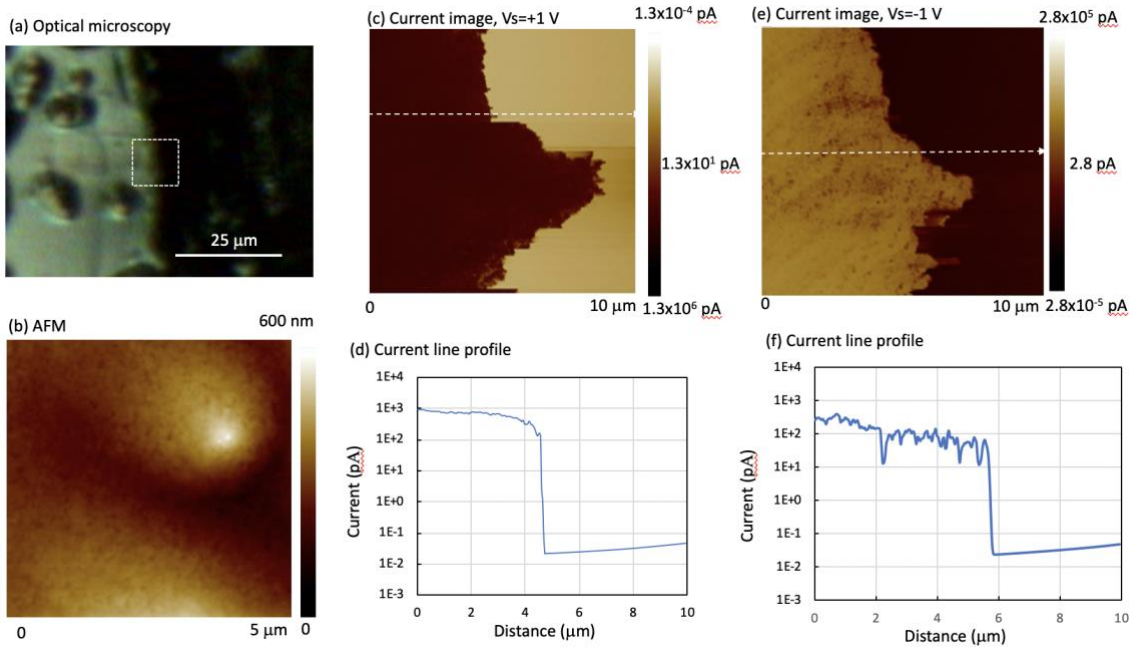

Fig. 5. Charge-transport images taken on a degraded area with highly mixed areas of ionic blocking and electronic shunting on the LICGC ceramic-only SSE after extensive cycling; (a) an optical microscopy image around this area; (b) an AFM surface morphology image simultaneously taken with the current images; (c) a current image taken with Vs = +1 V on the area as indicated by the square in the center of the optical image; (d) a current line profile along the line in (c); (e) a current image taken with Vs = -1 V in the same area as (b) and (c); and (f) a current line profile along the line in (e).

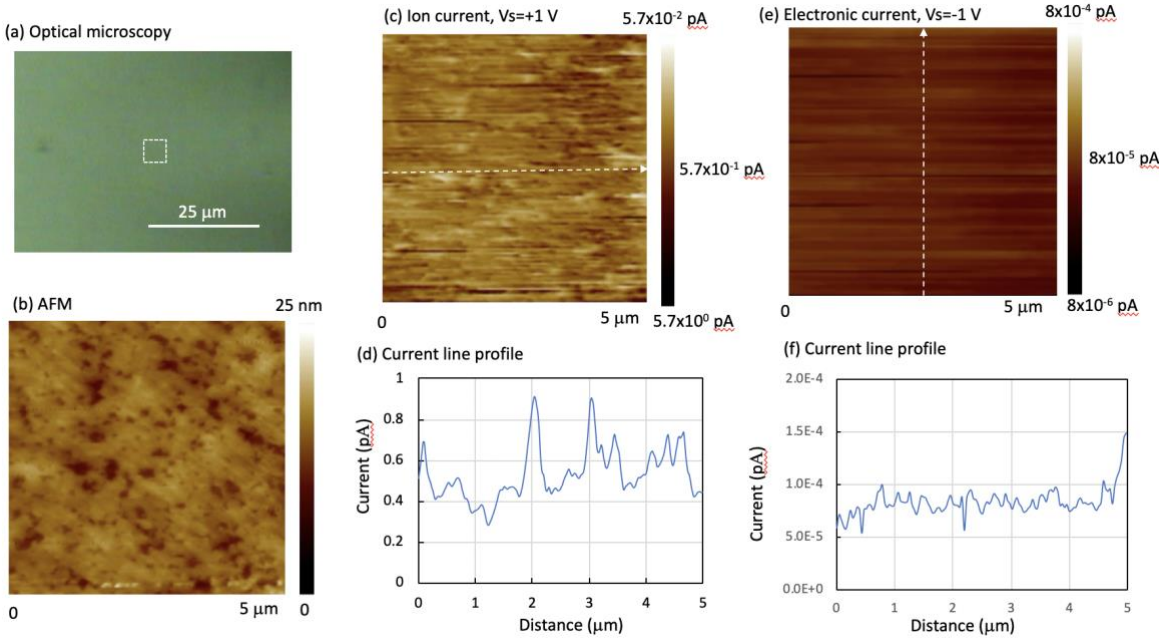

Fig. 6. Transport imaging of the pristine LICGC SSE with Li-containing PAN-coating; (a) an optical microscopy image; (b) an AFM surface morphology image simultaneously taken with the current images; (c) an ionic current image taken with Vs = +1 V on the area as indicated by the square in the center of the optical image; (d) a current line profile along the line in (c); (e) an electronic current image taken with Vs = -1 V in the same area as (b) and (c); and (f) a current line profile along the line in (e).

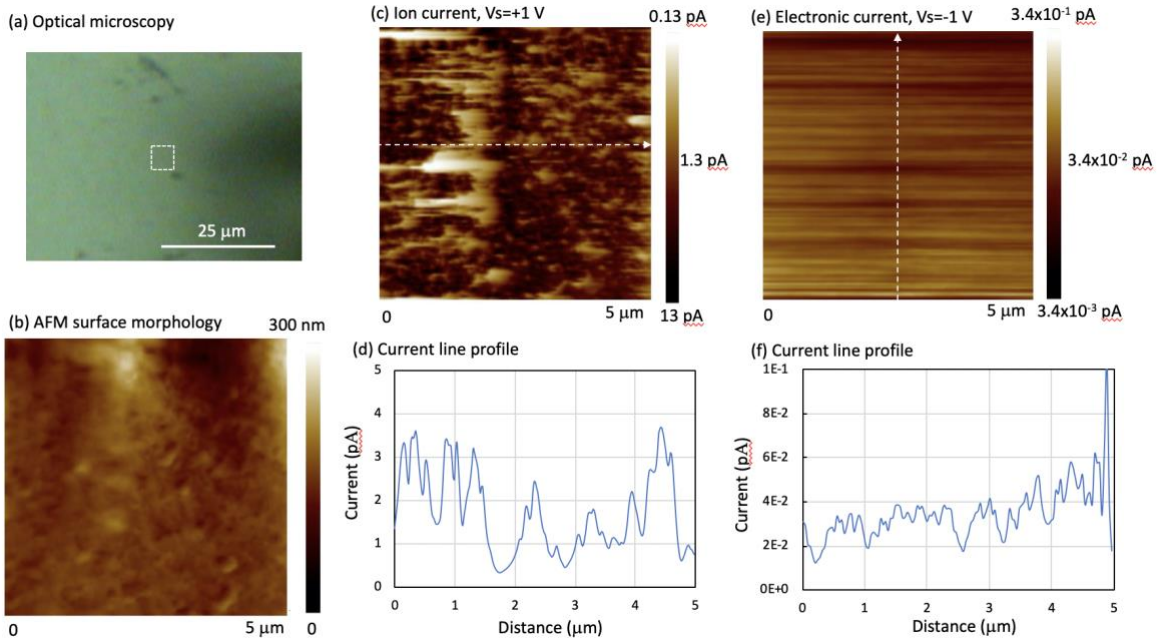

Fig. 7. Charge-transport images taken on a typical area of the LICGC SSE with the polymer coating after extensive cycling; (a) an optical microscopy image around this area; (b) an AFM surface morphology image simultaneously taken with the current images; (c) an ionic current image taken with Vs = +1 V on the area as indicated by the square in the center of the optical image; (d) a current line profile along the line in (c); (e) an electronic current image taken with Vs = -1 V in the same area as (b) and (c); and (f) a current line profile along the line in (e).

Supplementary materials

Local electrical degradations of solid-state electrolyte by nm-scale *operando* imaging of ionic and electronic transports

C.-S. Jiang[1]* Y. Yin[1], H. Guthrey[1], K. Park[1], S.-H. Lee[2], and M.M. Al-Jassim[1]

[1]National Renewable Energy Laboratory (NREL), Golden, Colorado, USA

[2]Department of Mechanical Engineering, University of Colorado, Boulder, USA

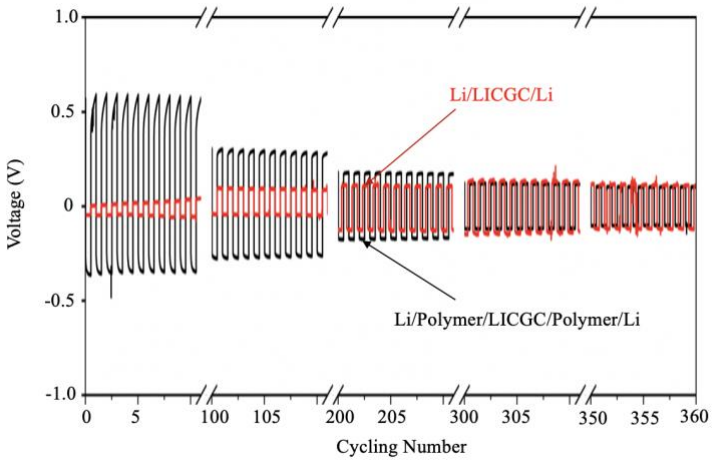

Fig. S1. Voltage profile of the Li/LiCGC/Li and Li/polymer/LiCGC/polymer/Li cells during stripping/plating cycling with a constant current density of 0.3 μA/cm^2.

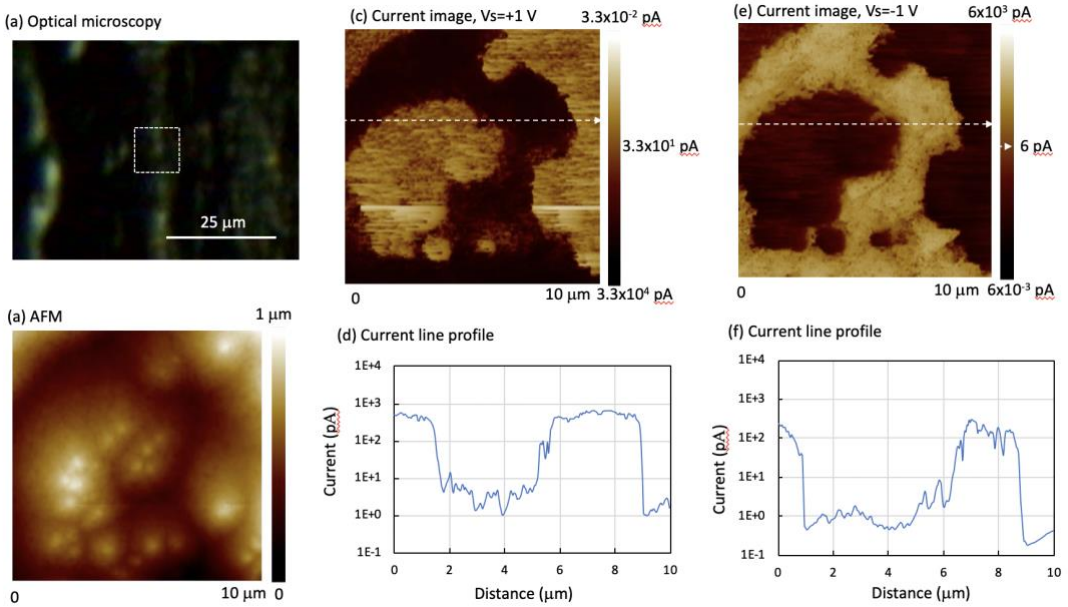

Fig. S2. Charge-transport images taken on a degraded area with highly blended areas of ionic blocking and electronic shunting on the LICGC ceramic-only SSE after extensive cycling; (a) an optical microscopy image around this area; (b) an AFM surface morphology image simultaneously taken with the current images; (c) a current image taken with Vs = +1 V on the area as indicated by the square in the center of the optical image; (d) a current line profile along the line in (c); (e) a current image taken with Vs = -1 V in the same area as (b) and (c); and (f) a current line profile along the line in (e).